GEOPHYSICS®

Accurate seismic dip and azimuth estimation using semblance dip guided structure-tensor analysis

SCHOLARONE™
Manuscripts

Accurate seismic dip and azimuth estimation using semblance dip guided structure-tensor analysis

Yihuai Lou[1], Bo Zhang[1], Tengfei Lin[2], Naihao Liu[3], Hao Wu[1], Rongchang Liu[1], and Danping Cao[4]

Right Running Head: Seismic dip and azimuth estimation

[1]The university of Alabama, Department of Geological Science. E-mail: ylou6@crimson.ua.edu;

bzhang33@ua.edu; hwu43@crimson.ua.edu; rliu22@crimson.ua.edu.

[2]Department of Middle East E&P, RIPED, CNPC. E-mail: lintf@petrochina.com.cn.

[3]Xi'an Jiaotong University, School of Electronic and Information Engineering. E-mail:

lnhfly@163.com

[4]China University of Petroleum (East China), School of Geoscience. E-mail:

caodp@upc.edu.cn.

Corresponding author:

Bo Zhang

Abstract

Seismic volumetric dip and azimuth are widely used in assisting seismic interpretation to depict geological structures such as chaotic slumps, fans, faults, and unconformities. Current popular dip and azimuth estimation methods include the semblance-based multiple window scanning method and gradient structure tensor (GST) analysis. However, the dip estimation accuracy using the semblance scanning method is affected by the dip of seismic reflectors. The dip estimation accuracy using GST analysis is affected by the analysis window centered at the analysis point. We proposed a new algorithm to overcome the disadvantages of dip estimation using multiple window scanning and GST analysis by combining and improving the two methods. The algorithm first obtains an estimated "rough" dip and azimuth for reflectors using the semblance scanning method. Then, the algorithm defines a window that is "roughly" parallel with the local reflectors using the estimated "rough" dip and azimuth. The algorithm next estimates the dip and azimuth of the reflectors within the analysis window using GST analysis. To improve the robustness of GST analysis to noise, we employ analytic seismic traces to compute the GST matrix. The algorithm finally employs Kuwahara window strategy to determine the dip and azimuth of local reflectors. To illustrate the superiority of this algorithm, we apply it to the F3 block poststack seismic data acquired in the North Sea, Netherlands. The comparison shows that the seismic volumetric dips estimated using our method more accurately follow the local seismic reflectors than dips computed from GST analysis and the semblance-based multiple window scanning method.

List of Key Words

Gradient structure tensor, multi-window technology, seismic volumetric dip

Introduction

The seismic volumetric dip and azimuth, which together reflect the orientations of seismic events, are important geometric attributes in assisting 3D seismic data interpretation. Four main categories exist for calculating seismic volumetric dip and azimuth. The first category is based on the cross-correlation. Bahorich and Farmer (1995) calculated the seismic volumetric dip by comparing the cross-correlation of a set of windowed seismic data, which was generated using time-lagging between nearby seismic traces. The second category uses a complex trace analysis to calculate the volumetric dip. Barnes (1996) and Luo et al. (1996) estimated the seismic dip by using the partial derivative of the instantaneous phase obtained from 3D complex trace analysis. To improve the stability of seismic dip estimation, Barnes (2000) smoothed the instantaneous phase using a weighted average window. Barnes (2007) further estimated the seismic dip by employing the ratio of smoothed instantaneous wavenumber to smooth instantaneous frequency. The third category is based on the semblance-based multiple window scanning method. Marfurt et al. (1998) first calculated semblance between the windowed seismic traces along a set of preset dips and azimuths and then treated the dip and azimuth pair that has the highest semblance value as the local reflector's dip and azimuth. Marfurt (2006) improved the accuracy of dip and azimuth estimation by using Kuwahara's multiple-window search. The fourth category is based on the gradient structure tensor (GST). The seismic volumetric dip and azimuth was estimated by utilizing the eigenvector that corresponds to the largest eigenvalue (Bakker et al., 1999; Fehmers and Hoecker, 2003). The GST resulted in inaccurate dip estimation when the sampling window encountered faults and other discontinuous structures. To improve the accuracy of the dip and azimuth estimation, Luo et al. (2006) used a data-adaptive weighting function to reformulate the GST. Wang et al. (2018) estimated the dip and azimuth by combining the GST analysis and

Kuwahara's multiple-window search strategy. Wu and Janson (2017) used directional structure tensors to estimate the seismic structural and stratigraphic orientations. Other methods, such as plane-wave destruction (Fomel, 2002), predictive painting (Fomel, 2010), and globally consistent dip estimation (Aarre, 2010), have been proposed to compute volumetric dip and azimuth.

The volumetric dip and azimuth are widely used to compute other geometric seismic attributes such as curvatures and similarity/coherence. The volumetric dip and azimuth can be used to improve the accuracy of the dip-steered coherence near steep structures (Marfurt et al., 1999). Barnes (2003) used the shaded relief seismic attribute, which combines reflectors dip and azimuth, to depict small-scale geologic structures. Al-Dossary and Marfurt (2006) used a partial derivative of reflectors dip to calculate the seismic curvature and further correlate seismic curvatures with fracture density. Lomask et al. (2006), Wu and Hale (2015; 2016), and Lou and Zhang (2018) used the reflector dip and azimuth to flatten the seismic reflection events and then generated a relative geologic time volume based on the flattened seismic volume. Wu and Fomel (2018) used reflection dips together with multi-grid correlations to calculate least-squares horizons. In addition, the seismic volumetric dip and azimuth are used for edge-preserving smoothing to detect sharp edges in seismic data, such as faults and other discontinuous structures (Luo et al., 2002; Qi et al., 2014; Wu and Guo, 2019; Lou et al., 2019). Structure-oriented filtering uses the volumetric dip and azimuth to suppress noise of both poststack and prestack seismic data and preserve edges of geologic structures (Hoecker and Fehmers, 2002; Zhang et al., 2016; Wu and Guo, 2019). Qi et al. (2016) employed a structure-oriented Kuwahara filter for seismic facies analysis. The reflector dip and azimuth are also used to incorporate structural constraints in geophysical inversion problems (Clapp et al. 2004; Wu 2017).

Multiple-window Kuwahara scanning and GST are among the most successful methods to estimate the dip and azimuth of seismic reflectors. The Kuwahara window search was developed by Kuwahara et al. (1976) to suppress random noise of image interior textures, but preserve texture edges. However, the multiple window scanning methods need users to define a set of dips and azimuths for the dip and azimuth scanning. Unfortunately, the user-defined increment of discrete candidate dip and azimuth may affect the accuracy of the dip and azimuth estimation. Computation costs increase with decreasing the interval of dips and azimuths. However, the accuracy of dip and azimuth estimation may decrease with increasing the interval of dips and azimuths, especially for the dip reflectors. Thus, it is very difficult to define a suitable interval of dips and azimuths for the whole seismic survey. GST-based methods treat the eigenvector (usually the first eigenvector) corresponding to the largest eigenvalue as the dip and azimuth of the local reflector. However, the correlation between the first eigenvector and dip and azimuth of local reflectors depends highly on the anisotropy of the windowed seismic image. The anisotropy of the seismic image is defined as the reflection patterns varying with different directions. An accurate dip and azimuth estimation can only be obtained if the extracted seismic events are the dominant linear feature within the analysis window. Thus, it is imperative that the seismic events within the defined window correspond to the most "dominant" linear feature (usually the first eigen value and eigen vectors) prior to the estimation of dip and azimuth using GST analysis. In this paper, we present a new method to estimate the seismic volumetric dip and azimuth robustly by integrating multiple-window Kuwahara scanning and GST analysis. We begin with generating a set of searching windows centered as the analysis point by rotating the analysis window along a user-defined dip and azimuth. Then, we calculate the semblance of seismic data in each analysis window. The window with highest semblance value is the best window for the following GST analysis. Using

the best window, we extract the seismic data and employ GST analysis to compute the dip and azimuth of seismic data. Finally, we employ the Kuwahara window search to determine the dip and azimuth of local seismic reflectors. Our method is applied to the poststack seismic survey in the F3 Block acquired in the North Sea, Netherlands.

Dip Estimation Using Multiple Window Scanning

Marfurt et al. (1999) proposed to estimate the dip of seismic reflectors using multiple window scanning (MWS), which begins with defining inline and crossline dip increment. We also need to define the minimum and maximum inline and crossline dips for scanning. Figure 1 shows the schematic diagram for a 2D dip estimation of the seismic reflector (Marfurt et al., 1999) with the yellow dot (intersection of yellow lines) as the analysis point. First, we extract the seismic data using a user-defined window centered at a set of discrete candidate dips (shown in orange, green, and blue) and compute the coherence for the extracted seismic data. In this example, we obtain the maximum coherence along the dip shown in green. Next, we pass an interpolation curve through the coherence measures estimated by the peak value and two or more neighboring dips. The peak value of this curve gives an estimate of coherence, whereas the corresponding dip value of the peak coherence gives an estimate of instantaneous dip.

To improve the robustness of dip and azimuth estimation to noise (Marfurt, et al., 1999), we employ complex seismic trace $F(t,x,y)$ in the following analysis. The complex seismic trace $F(t,x,y)$ is defined as

$$F(t,x,y) = f(t,x,y) + if^{H}(t,x,y) \tag{1}$$

where f^{H} is the Hilbert transform of the real seismic trace, f ; t is the two-way travel time; x and y are the inline and crossline coordinates, respectively. We calculate the coherence $S(k,l)$ for the analysis point in every analysis window using the semblance-based coherence (Marfurt et al., 1998)

$$S(k,l) = \frac{\sum\limits_{m_t=-M_t}^{+M_t} \left\{ \left[\sum\limits_{n=1}^{N} f(\tau_0 + m_t, x, y) \right]^2 + \left[\sum\limits_{n=1}^{N} f^H(\tau_0 + m_t, x, y) \right]^2 \right\}}{N \sum\limits_{m_t=-M_t}^{+M_t} \sum\limits_{n=1}^{N} \left\{ [f(\tau_0 + m_t, x, y)]^2 + [f^H(\tau_0 + m_t, x, y)]^2 \right\}}, \tag{2}$$

where M_t is the half window size in number of samples; k and l are the dip indexes in inline and crossline directions, respectively; N is the number of seismic traces in the analysis window; τ_0 is the time index corresponding to t_0. We use (X) to represent (t, x, y) in the following analysis.

Figure 2 shows a representative inline seismic section within the F3 seismic survey. Figures 3a, and 3b show the computed crossline dip varying with the increment of discrete scanning dips at the analysis points marked by red, and blue crosses, respectively, in Figure 2. The size of the time window is 9 samples centered at the analysis points. The minimum and maximum scanning dips are -0.32 ms/m, 0.32 ms/m. The increment of the discrete scanning dips ranges from 0.016 ms/m to 0.08 ms/m. Figure 3a illustrates that the increment of the discrete scanning dips has negligible effect on the dip estimation for the reflectors with gentle dip angles. Figures 3b shows that there is noticeable variation of the estimated dips varying with increment of scanning dips. The phenomenon in Figures 3a, and 3b demonstrates that the effect of the increment of discrete scanning dips on the dip estimation for the reflectors increases with increasing dip angle of the seismic reflectors.

Dip Estimation by Applying GST Analysis to Analytical Seismic Traces

In Figure 4a, the red window shows the extracted traces (red dots) used for the dip estimation using GST analysis. We obtain the dip of the reflectors by analyzing the eigenvector of gradient tensor computed using the extracted seismic traces. Unfortunately, dip estimation accuracy highly depends on the anisotropy of the seismic image. As a result, the dip of the reflectors may affect the accuracy of the dip estimation using GST analysis. To demonstrate this

issue, we first extract the seismic data using time windows along discrete number of candidate dips (Figures 4b and 4c) and then compute the dip of the extracted seismic data using GST analysis. The reflectors dip θ at this analysis point is

$$\theta = \theta_1 + \theta_2 \tag{3}$$

where θ_1 and θ_2 are the dips of discrete window used to extracted the seismic data, and the estimated dip of the reflectors of the extracted seismic data, respectively.

To improve the stability of the dip estimation using GST analysis to noise, we use analytical seismic traces to construct the structure tensor. First we generate the gradient vector $\mathbf{V}_s(\mathbf{X})$ for each sample of the seismic traces by using the partial derivatives $\dfrac{\partial F(\mathbf{X})}{\partial t}$, $\dfrac{\partial F(\mathbf{X})}{\partial x}$, and $\dfrac{\partial F(\mathbf{X})}{\partial y}$:

$$\mathbf{V}_s(\mathbf{X}) = \left[\frac{\partial F(\mathbf{X})}{\partial t} \quad \frac{\partial F(\mathbf{X})}{\partial x} \quad \frac{\partial F(\mathbf{X})}{\partial y} \right]^T \tag{4a}$$

$$\frac{\partial F(\mathbf{X})}{\partial t} = 0.5 * f(\tau_0, x, y) * \left(f^H(\tau_0 + 1, x, y) - f^H(\tau_0 - 1, x, y) \right) \\ - 0.5 * f^H(\tau_0, x, y) * \left(f(\tau_0 + 1, x, y) - f(\tau_0 - 1, x, y) \right) \tag{4b}$$

$$\frac{\partial F(\mathbf{X})}{\partial x} = 0.5 * f(\tau_0, x, y) * \left(f^H(\tau_0, x + 1, y) - f^H(\tau_0, x - 1, y) \right) \\ - 0.5 * f^H(\tau_0, x, y) * \left(f(\tau_0, x + 1, y) - f(\tau_0, x - 1, y) \right) \tag{4c}$$

$$\frac{\partial F(\mathbf{X})}{\partial y} = 0.5 * f(\tau_0, x, y) * \left(f^H(\tau_0, x, y + 1) - f^H(\tau_0, x, y - 1) \right) \\ - 0.5 * f^H(\tau_0, x, y) * \left(f(\tau_0, x, y + 1) - f(\tau_0, x, y - 1) \right) \tag{4d}$$

The gradient structure tensor $\mathbf{GST}(\mathbf{X})$ at the analysis point $(\mathbf{X})$ is given by

$$\mathbf{GST}(\mathbf{X}) = \sum_{m_x = -M_x}^{M_x} \sum_{m_y = -M_y}^{M_y} \sum_{m_t = -M_t}^{M_t} W(\mathbf{X} + \mathbf{M}) * \mathbf{V}_s(\mathbf{X} + \mathbf{M}) * \mathbf{V}_s^T(\mathbf{X} + \mathbf{M}) \tag{5}$$

where M_x and M_y are the half size of the analysis window along inline and crossline directions; $\mathbf{M}$ represents $\left(m_t, m_x, m_y\right)$; $W(\mathbf{X})$ is the weighting factor to enhance the signal to noise ratio (Luo et al. 2006). Then, we calculate the eigenvalues and eigenvectors of the structure tensor

$$GST(X) = \lambda_u(X)u(X)u^T(X) + \lambda_v(X)v(X)v^T(X) + \lambda_w(X)w(X)w^T(X), \tag{6}$$

where $\lambda_u(\mathbf{X}), \lambda_v(\mathbf{X}), \lambda_w(\mathbf{X})$ are eigenvalues satisfied $\lambda_u(\mathbf{X}) \geq \lambda_v(\mathbf{X}) \geq \lambda_w(\mathbf{X}) \geq 0$. $u(\mathbf{X}), v(\mathbf{X})$ and $w(\mathbf{X})$ are the corresponding normalized eigenvectors. The dominant eigenvector $u(\mathbf{X})$ corresponding to the largest eigenvalues is perpendicular to the local reflectors. Therefore, the inline dip $p(k,l)$ and crossline dip $q(k,l)$ of the seismic reflector within the analysis window are defined as

$$p(k,l) = \frac{u_x(\mathbf{X})}{u_t(\mathbf{X})} \tag{7}$$

$$q(k,l) = \frac{u_y(\mathbf{X})}{u_t(\mathbf{X})} \tag{8}$$

If the inline dip and crossline dip of the discrete search window are θ_k and θ_l, respectively, then the inline dip $P(k,l)$ and crossline dip $Q(k,l)$ of the seismic reflector at the analysis point are defined as

$$P(k,l) = p(k,l) + \theta_k, \tag{9}$$

$$Q(k,l) = q(k,l) + \theta_l. \tag{10}$$

Figures 4a, 4b, and 4c show three discrete windows used to extract the seismic traces needed for the construction of the structure tensor. Figure 4a shows a traditional time window for the GST analysis. The estimated dip (θ_2) for the extracted seismic traces in Figure 4a is the dip of the reflector at the analysis point. The dip of the window used to extract the seismic traces in Figure

4b has an opposite dip with the dip of the seismic reflection. Thus, the dip angle (θ_2) of the extracted seismic traces is larger than the dip of the seismic reflection at the analysis point. The dip of the window used to extract the seismic traces in Figure 4c is approximately same as the dip of the seismic reflection. Thus, the dip angle (θ_2) of the extracted seismic traces in Figure 4c approximately equals to 0 ms/m. Figure 4d shows the computed dip θ at the analysis point labeled by the blue cross shown in Figure 2 varying with dips of the analysis window. The dip value labeled by the green dot in Figure 4d is estimated using an analysis window, which is approximately parallel to the local seismic events. The dip value labeled by the red dot in Figure 4d is estimated using an analysis window which has 0 ms/m dip angle (the traditional window). Ideally, the estimated dip θ at the analysis point should be a constant value for all analysis windows if the anisotropy value of seismic images is 0. However, Figure 4d illustrates that we obtain different dip estimations if we use different analysis windows. Thus, the reflectors dip estimated using GST analysis is highly dependent on how seismic data are extracted. Figure 4d also illustrates that there is negligible variation of dip values if the analysis windows are approximately parallel with the dip of the local reflectors. Figures 5, and 6 show the dips estimated using GST analysis as a function of discrete candidate analysis windows for the red, and blue crosses, respectively, in Figure 2. The X-axis and Y-axis in Figures 5, and 6 are inline dip θ_k and crossline dip θ_l of the analysis window, respectively. Figures 5a and 5b show the computed inline dip $P(k,l)$ and crossline dip $Q(k,l)$ at the analysis point marked by the red cross in Figure 2. Figures 6a and 6b show the computed inline dip $P(k,l)$ and crossline dip $Q(k,l)$ at the analysis point marked by the blue cross in Figure 2. At these two analysis points, the estimated inline and crossline dips are a function of the analysis window parameters (θ_k, θ_l) used for extracting the seismic data. The rate of estimated dips varies with the parameters of the analysis window,

indicating that the way we extracted the seismic data affects the dip estimation result. The white dots in Figures 5, and 6 indicate the analysis windows, which are approximately parallel with the surface of the local reflectors.

Dip Estimation by Integrating Discrete Window Scanning and GST Analysis

Figure 7 shows the workflow of our method. Our method begins with rotating the analysis window along a set of user-defined dips and azimuths. Next, we calculate the semblance in every analysis window. Considering that the GST analysis may result in inaccurate dip estimation when the analysis window does not follow the local reflector, we select the window that is approximately parallel to the local seismic events as the analysis window for GST analysis. In this paper, we employ the semblance scanning strategy to find the window which is approximately parallel to the local reflector. Next, we compute the dip and azimuth of the seismic events within the selected window using GST analysis. Finally, we output the dip, azimuth, and coherence of the analysis point using Kuwahara searching (Marfurt, 2006).

Real Data Examples

To illustrate the effectiveness of our method, we apply it to a poststack seismic volume (F3 block) acquired in the North Sea, Netherlands. The F3 block seismic data consists of 400 inline and 700 crossline. The inline and crossline interval is 25m and the time increment of the seismic traces is 4ms. We compare the volumetric dip computed using our method with other two methods.

Figure 8 shows a representative inline seismic section within the 3D seismic survey. The red line AA' in Figure 8 indicates the location of the inline section within the seismic survey (rectangle in upper right corner of the figure). The yellow line BB' in Figure 8 indicates the two-way travel time of the analyzed time slice across the salt dome shown in Figure 12. Figures 9a, 9b, and 9c show the computed crossline dips using multiple window scanning (Marfurt, 2006), GST analysis,

and our method, respectively. The increment of the discrete scanning candidate dips is 0.016 ms/m for both inline and crossline dip estimation. We choose two representative reflection features in Figure 8 to illustrate the superiority of our method. Steep crossline dip angles are present for the seismic reflections within the black rectangle and "sinusoidal" shapes and chaotic features within the blue rectangle (Figure 8). Figures 10a, 10b, and 10c show the zoomed-in seismic amplitude (blue rectangle, Figure 8) co-rendered with the crossline dip computed using multiple window scanning, GST analysis, and our method, respectively. In Figure 10a, the dip computed using the scanning method smears across discontinuous zones indicated by white arrows. In Figure 10b, the estimated dip using GST analysis has abrupt changes (color changing from red to dark blue) for the seismic reflection indicated by the red arrow, indicating that the GST based method may give us an inaccurate dip estimation of seismic reflectors. However, our method accurately estimates the reflectors dip near discontinuous zones indicated by red and white arrows (Figure 10c). Figures 11a, 11b, and 11c show the zoomed-in seismic amplitude (black rectangle, Figure 8) co-rendered with the crossline dip computed using multiple window scanning, GST analysis, and our method, respectively. In Figure 11a, inaccurate dip estimations are indicated by white arrows and artifacts are indicated by red arrows. The estimated dip using GST analysis (Figure 11b) is overall smaller than that shown in Figure 11a for the reflections on the salt dome flank (steep angle structures). The two reflection events indicated by white arrows in Figure 11b are visually parallel to each other. Thus, we should have almost same color (dip angle) for those two reflection events. However, in Figure 11b, seismic reflections indicated by the lower white arrow has a deeper red color than seismic reflections indicated by the upper white arrow. The seismic reflections indicated by the purple arrow in Figure 11b are parallel with each other. They should have same color (dip angle) for all seismic reflections. However, we have slightly different colors for different samples

within the seismic reflections. By comparison, our method accurately estimates the reflector's dip for both structures with steep dipping angle and other seismic reflections indicated by arrows in the Figure 11c.

Figure 12 shows a representative time slice of seismic amplitude across the salt dome along the yellow line BB' in Figure 8. Seismic amplitude co-rendered with crossline dips are shown on Figures 13a, 13b, and 13c and with inline dips on Figures 14a, 14b, and 14c computed using multiple window semblance scanning, GST analysis, and our method. The inline and crossline dips computed from multiple window scanning have more noise (zones indicated by black arrows in Figures 13a, 13c, 14a, and 14c) when compared to that computed using our method. In Figures 13 and 14, white arrows indicate locations where there are steep reflections. The dip angle computed using GST analysis is smaller than that computed using both of the other two methods.

Then, we illustrate the superiority of our method by comparing the structure curvatures (Al-Dossary and Marfurt, 2006), which are computed from the estimated dips accordingly. Figures 15a, 15b, and 15c show the time slices of the most positive curvature derived from dips computed using semblance (Figures 13a and 14a), GST analysis (Figures 13b and 14b), and our method (Figures 13c and 14c), respectively. The black arrows in Figures 15a, 15b, and 15c indicate representative locations at the salt dome boundary. The smeared curvature anomalies across the salt dome boundary are indicated by black arrows in Figures 15a and 15b. However, the curvature anomalies in Figure 15c illustrate sharp features at the salt dome boundary. The white arrows in Figures 15a, 15b, and 15c show the representative locations where the curvature computed from new dips shows more continuous anomalies at the salt dome boundary than those computed from the dips estimated using semblance and GST analysis. In this paper, we only compare the most

positive curvatures computed from the three different dips; however, we can obtain similar results by comparing other curvature measurements, such as the most negative curvature.

Conclusion

In this paper, we propose a new method to improve the accuracy of volumetric dip estimation. A proper increment of discrete candidate angles is one of the most important parameters for the dip estimation using multiple window scanning. The dip estimated using GST analysis is usually smaller than the dip of seismic reflectors. Our workflow avoids the inaccurate dip estimation near discontinuous and steep structure zones by integrating the advantages of the multiple window scanning and GST analysis. We improve the accuracy of dip estimation by applying GST analysis to the window, which is approximately parallel to the local seismic reflector. We employ the multiple window scanning method to find the window that is approximately parallel to the local seismic reflector. Field data examples show that our method precisely estimates reflectors dip near steep structures. The field data application also demonstrates that the dip estimated using our method has better anti-noise performance, and the structure curvature generated using our method precisely highlights the boundary of the salt dome.

Reference

Aarre, V., 2010, Globally consistent dip estimation: SEG Technical Program Expanded Abstracts 2010, 1387-1391.

Al-Dossary, S. and K. J. Marfurt, 2006, 3D volumetric multispectral estimates of reflector curvature and rotation: Geophysics, **71**(5), P41-P51.

Bahorich, M., and S. Farmer, 1995, 3D seismic discontinuity for faults and stratigraphic features: The coherence cube: The Leading Edge, **14**(10), 1053-1058.

Bakker, P., L. J. van Vliet, and P. W. Verbeek, 1999, Edge-preserving orientation adaptive filtering: IEEE Computer Society Conference on Computer Vision and Pattern Recognition, 1, 535-540.

Barnes, A. E., 1996, Theory of 2-D complex seismic trace analysis: Geophysics, **61**(1), 264-272.

Barnes, A. E., 2000, Weighted average seismic attributes: Geophysics, **65**(1), 275-285.

Barnes, A. E., 2003, Shaded relief seismic attribute: Geophysics, **68**(4), 1281-1285.

Barnes A. E., 2007, A tutorial on complex seismic trace analysis: Geophysics, **72**(6), W33-W43.

Clapp, R. G., B. Biondi, and J. F. Claerbout, 2004, Incorporating geologic information into reflection tomography: Geophysics, **69**(2), 533–546.

Fehmers, G. C., and C. F. Höcker, 2003, Fast structural interpretation with structure-oriented filtering: Geophysics, **68**(4), 1286-1293.

Fomel, S., 2002, Applications of plane-wave destruction filters: Geophysics, **67**(6), 1946–1960.

Fomel, S., 2010, Predictive painting of 3-D seismic volumes: Geophysics, **75**(4), A25–A30.

Hoecker, C., and G. Fehmers, 2002, Fast structural interpretation with structure-oriented filtering: The Leading Edge, **21**(3), 238-243.

Kuwahara, M., K. Hachimura, S. Eiho, and M. Kinoshita, 1976, Processing of RI-angiocardiographic images: Digital processing of biomedical images, 187-202.

Lomask, J., A. Guitton, S. Fomel, J. Claerbout, and A. A. Valenciano, 2006, Flattening without picking: Geophysics, **71**(4), P13-P20.

Lou, Y., and B. Zhang, 2018, Automatic horizon picking using multiple seismic attributes: SEG Technical Program Expanded Abstracts 2018, 1683-1687.

Lou, Y., B. Zhang, R. Wang, T. Lin, and D. Cao, 2019, Seismic Fault Attribute Estimation Using a Local Fault Model: Geophysics, **84**(4), 1-44.

Luo, Y., W. G. Higgs, and W. S. Kowalik, 1996, Edge detection and stratigraphic analysis using 3D seismic data: SEG Technical Program Expanded Abstracts 1996, 324-327.

Luo, Y., M. Marhoon, S. Al-Dossary, and M. Alfaraj, 2002, Edge-preserving smoothing and applications: The Leading Edge, **21**(2), 136–158

Luo, Y., Y. E. Wang, N. M. AlBinHassan, and M. N. Alfaraj, 2006, Computation of dips and azimuths with weighted structural tensor approach: Geophysics, **71**(5), V119-V121

Marfurt, K. J., 2006, Robust estimates of 3D reflector dip and azimuth: Geophysics, **71**(4), P29-P40.

Marfurt, K. J., R. L. Kirlin, S. L. Farmer, and M. S. Bahorich, 1998, 3D seismic attributes using a running window semblance-based algorithm: Geophysics, **63**(4), 1150-1165.

Marfurt, K. J., V. Sudhakar, A. Gersztenkorn, K. D. Crawford, and S. E. Nissen, 1999, Coherency calculations in the presence of structural dip: Geophysics, **64**(1), 104-111

Qi, J., B. Zhang, H. Zhou, and K. J. Marfurt, 2014, Attribute expression of fault-controlled karst - Fort Worth Basin, TX: Interpretation, **2**(3), SF91–SF110.

Qi, J., T. Lin, T. Zhao, F. Li, and K. J. Marfurt, 2016, Semisupervised multiattribute seismic facies analysis: Interpretation, **4**(1), SB91-SB106.

Wang, X., W. Chen, and Z. Zhu, 2018, Robust Seismic Volumetric Dip Estimation Combining Structure Tensor and Multiwindow Technology: IEEE Transactions on Geoscience and Remote Sensing, 99, 1-11.

Wu, X., 2017, Structure-, stratigraphy- and fault-guided regularization in geophysical inversion: Geophysical Journal International, **210**(1), 184-195.

Wu, X. and D. Hale, 2015, Horizon volumes with interpreted constraints: Geophysics, **80**(2), IM21-IM33.

Wu, X. and D. Hale, 2016, Automatically interpreting all faults, unconformities, and horizons from 3D seismic images: Interpretation, **4**(2), T227-T237.

Wu, X. and S. Fomel, 2018, Least-squares horizons with local slopes and multi-grid correlations: Geophysics, **84**(4), IM29-IM40.

Wu, X. and Z. Guo, 2019, Detecting faults and channels while enhancing seismic structural and stratigraphic features: Interpretation, **7**(1), T155-T166.

Wu, X. and X., Janson, 2017, Directional structure tensors in estimating seismic structural and stratigraphic orientations: Geophysical Journal International, **210**(1), 534-548

Zhang, B., T. Lin, S. Guo, O.E. Davogustto, and K.J. Marfurt, 2016, Noise suppression of time-migrated gathers using prestack structure-oriented filtering: Interpretation, **4**(2), pp.SG19-SG29.

List of figure captions

Figure 1. Schematic showing the 2D semblance scanning method (Modified from Marfurt, 2006).

Figure 2. A representative inline seismic section with two analysis points (red and blue crosses). Computed dips of red and blue crosses are shown in Figures 3a and 3b, respectively.

Figure 3. The computed dip varying with the increment of discrete scanning dips at the analysis points indicated by (a) the red cross, (b) the blue cross in Figure 2.

Figure 4. The computed dip as a function of discrete candidate analysis windows. (a) The discrete candidate window along the 0 degree (the traditional GST window). (b) The discrete candidate window along the minimum scanning degree. (c) The discrete candidate window along the dip approximately parallel to local seismic reflectors. (d) The computed dip for the analysis point.

Figure 5. The computed (a) inline dip and (b) crossline dip at analysis point indicated by the red cross in Figure 2. The computed dips are a function of discrete candidate analysis windows.

Figure 6. The computed (a) inline dip and (b) crossline dip at analysis point indicated by the blue cross in Figure 2. The computed dips are a function of discrete candidate analysis windows.

Figure 7. Workflow for the dip estimation by integrating discrete window scanning and GST analysis.

Figure 8. The representative inline seismic section, depicting a salt dome in the black rectangle.

Figure 9. Compare estimated crossline dip of different methods for the inline seismic section in Figure 8. Dip estimations based on (a) semblance scanning method, (b) GST analysis, and (c) our proposed method. Black and blue rectangles are two representative reflection features used to illustrate the superiority of our method.

Figure 10. The zoomed-in estimated dip in the blue rectangle in Figure 9 overlay on the zoomed-in seismic section in the blue box in Figure 8. Dip estimations based on (a) semblance scanning

method, (b) GST analysis, and (c) our proposed method. White arrows in Figure 10a indicate estimated dip smears across discontinuous zones. Red arrow in Figure 10b indicates the inaccurate dip estimation. Red and white arrows in Figure 10c indicate our method accurately estimates the reflectors dip near discontinuous zones.

Figure 11. The zoomed-in estimated dip in the black rectangle in Figure 9 overlay on the zoomed-in seismic section in the black box in Figure 8. Dip estimations based on (a) semblance scanning method, (b) GST analysis, and (c) our proposed method. White and red arrows in Figure 11a indicate inaccurate estimated dips and artifacts, respectively. Purple and white arrows in Figure 11b indicate seismic reflections should have the same color, and almost the same color, respectively. The arrows in Figure 11c indicate our method accurately estimates the reflectors dip.

Figure 12. The representative time slice seismic dataset at 1650ms.

Figure 13. Time slice at 1650ms from the crossline dip volume (equivalent to the time slice in Figure 12). Dip estimations based on (a) semblance scanning method, (b) GST analysis, and (c) our proposed method. White and black arrows indicate steep reflections, and locations with noise, respectively.

Figure 14. Time slice at 1650ms from the inline dip volume (equivalent to the time slice in Figure 12). Dip estimations based on (a) semblance scanning method, (b) GST analysis, and (c) our proposed method. White and black arrows indicate steep reflections, and locations with noise, respectively.

Figure 15. Time slice at 1650ms from the most positive curvature volume (equivalent to the time slice in Figure 12). The most positive curvature based on the dip computed using (a) semblance scanning method, (b) GST analysis, and (c) our proposed method. White and black arrows indicate representative locations at the salt dome boundary.
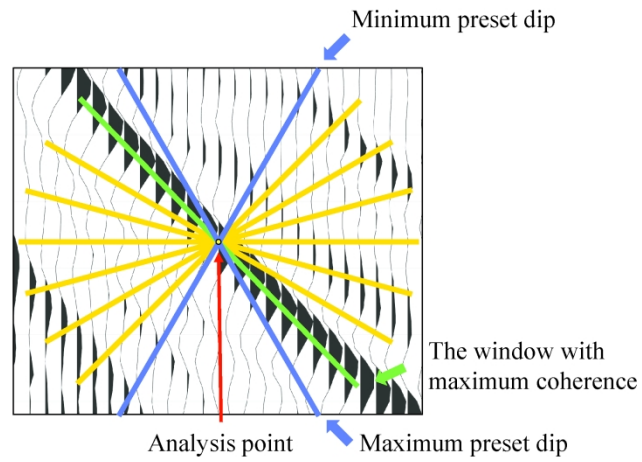
Figure 1.

Figure 1. Schematic showing the 2D semblance scanning method (Modified from Marfurt, 2006).

254x190mm (300 x 300 DPI)
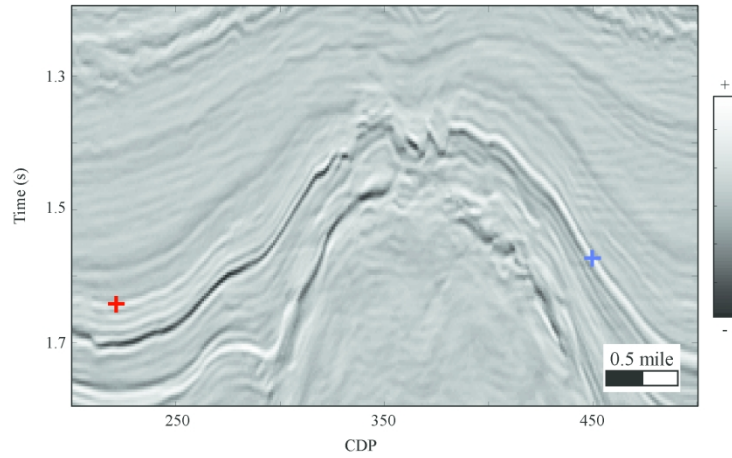
Figure 2.

Figure 2. A representative inline seismic section with two analysis points (red and blue crosses). Computed dips of red and blue crosses are shown in Figures 3a and 3b, respectively.

254x190mm (300 x 300 DPI)
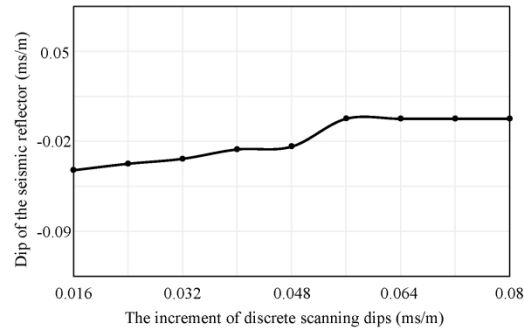
Figure 3a.

Figure 3a. The computed dip varying with the increment of discrete scanning dips at the analysis points indicated by (a) the red cross, (b) the blue cross in Figure 2.

254x190mm (300 x 300 DPI)
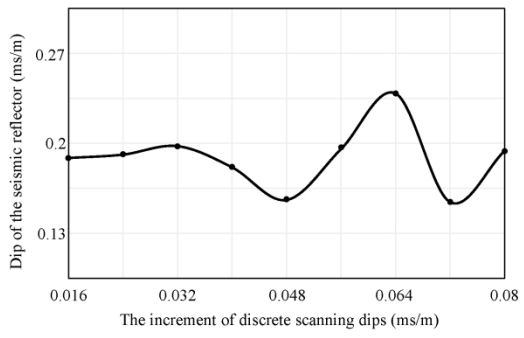
Figure 3b.

Figure 3b. The computed dip varying with the increment of discrete scanning dips at the analysis points indicated by (a) the red cross, (b) the blue cross in Figure 2.

254x190mm (300 x 300 DPI)
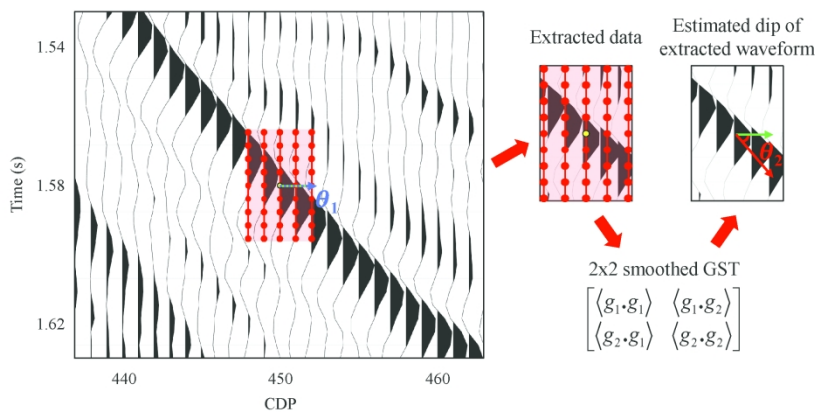
Figure 4a.

Figure 4a. The computed dip as a function of discrete candidate analysis windows. (a) The discrete candidate window along the 0 degree (the traditional GST window). (b) The discrete candidate window along the minimum scanning degree. (c) The discrete candidate window along the dip approximately parallel to local seismic reflectors. (d) The computed dip for the analysis point.

254x190mm (300 x 300 DPI)
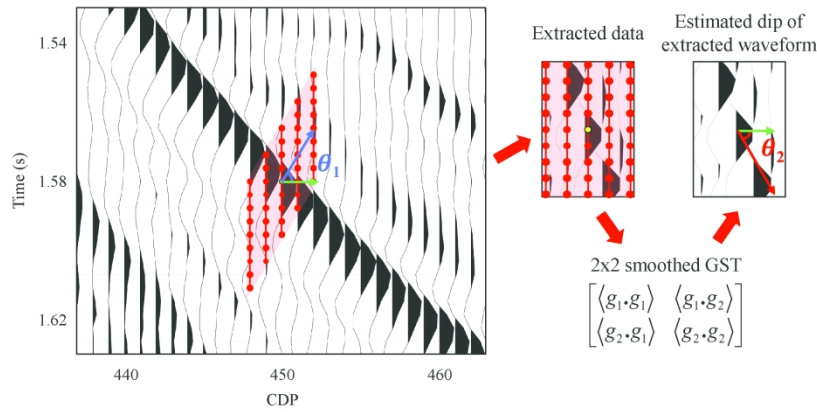
Figure 4b.

Figure 4b. The computed dip as a function of discrete candidate analysis windows. (a) The discrete candidate window along the 0 degree (the traditional GST window). (b) The discrete candidate window along the minimum scanning degree. (c) The discrete candidate window along the dip approximately parallel to local seismic reflectors. (d) The computed dip for the analysis point.

254x190mm (300 x 300 DPI)
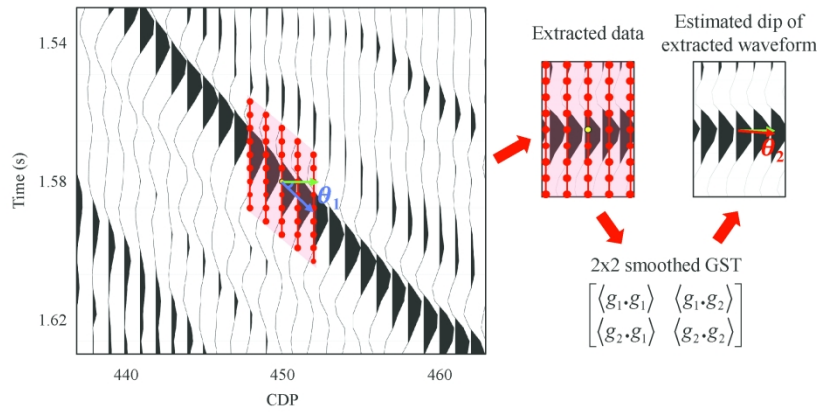
Figure 4c.

Figure 4c. The computed dip as a function of discrete candidate analysis windows. (a) The discrete candidate window along the 0 degree (the traditional GST window). (b) The discrete candidate window along the minimum scanning degree. (c) The discrete candidate window along the dip approximately parallel to local seismic reflectors. (d) The computed dip for the analysis point.

254x190mm (300 x 300 DPI)
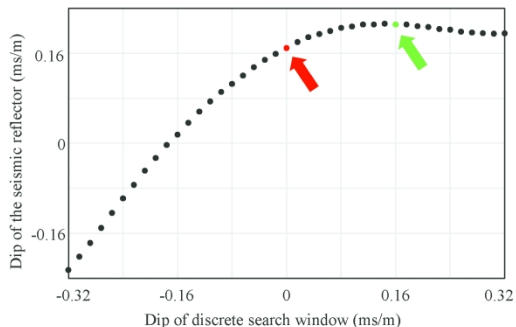
Figure 4d.

Figure 4d. The computed dip as a function of discrete candidate analysis windows. (a) The discrete candidate window along the 0 degree (the traditional GST window). (b) The discrete candidate window along the minimum scanning degree. (c) The discrete candidate window along the dip approximately parallel to local seismic reflectors. (d) The computed dip for the analysis point.

254x190mm (300 x 300 DPI)
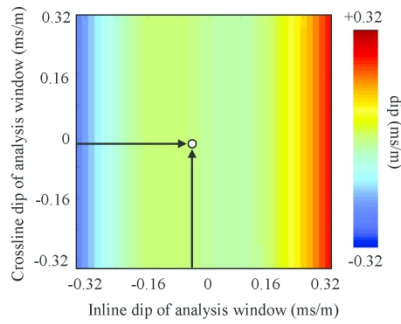
Figure 5a.

Figure 5a. The computed (a) inline dip and (b) crossline dip at analysis point indicated by the red cross in Figure 2. The computed dips are a function of discrete candidate analysis windows.

254x190mm (300 x 300 DPI)
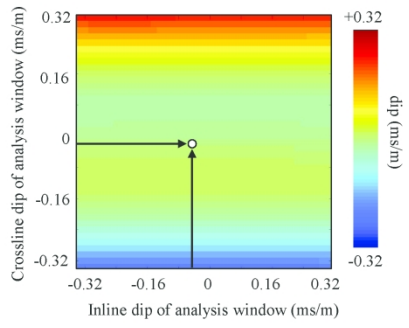
Figure 5b.

Figure 5b. The computed (a) inline dip and (b) crossline dip at analysis point indicated by the red cross in Figure 2. The computed dips are a function of discrete candidate analysis windows.

254x190mm (300 x 300 DPI)
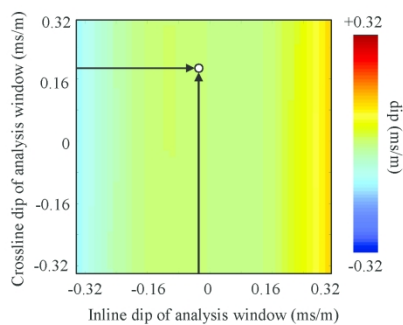
Figure 6a.

Figure 6a. The computed (a) inline dip and (b) crossline dip at analysis point indicated by the blue cross in Figure 2. The computed dips are a function of discrete candidate analysis windows.

254x190mm (300 x 300 DPI)
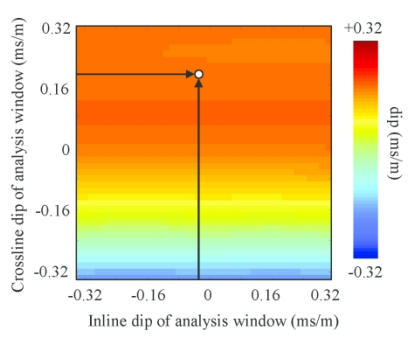
Figure 6b.

Figure 6b. The computed (a) inline dip and (b) crossline dip at analysis point indicated by the blue cross in Figure 2. The computed dips are a function of discrete candidate analysis windows.

254x190mm (300 x 300 DPI)
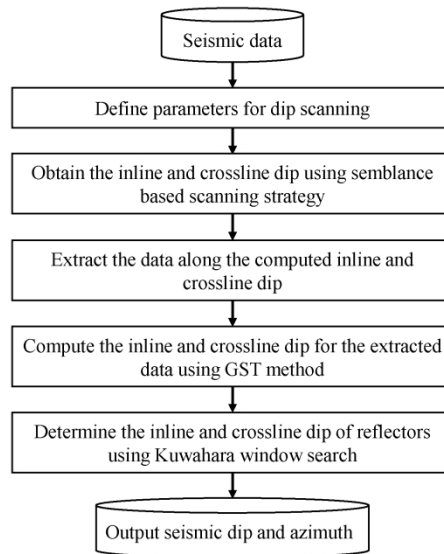
Figure 7.

Figure 7. Workflow for the dip estimation by integrating discrete window scanning and GST analysis.

254x190mm (300 x 300 DPI)
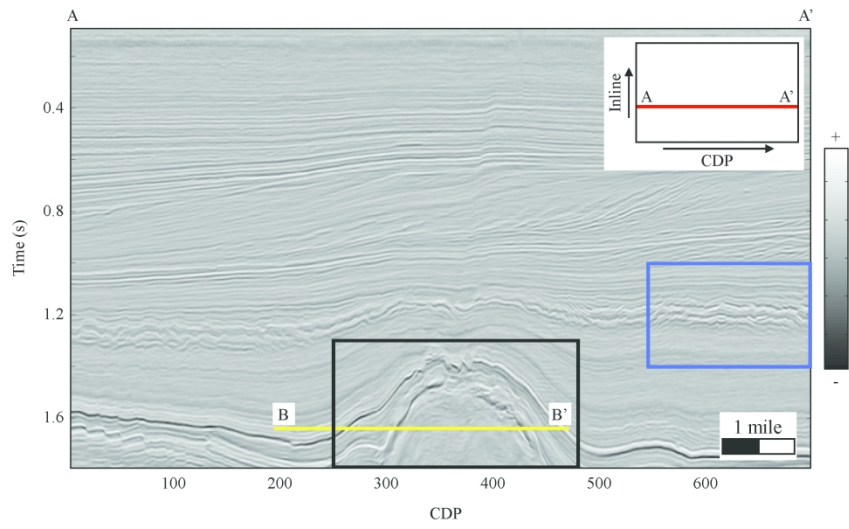
Figure 8.

Figure 8. The representative inline seismic section, depicting a salt dome in the black rectangle.

254x190mm (300 x 300 DPI)
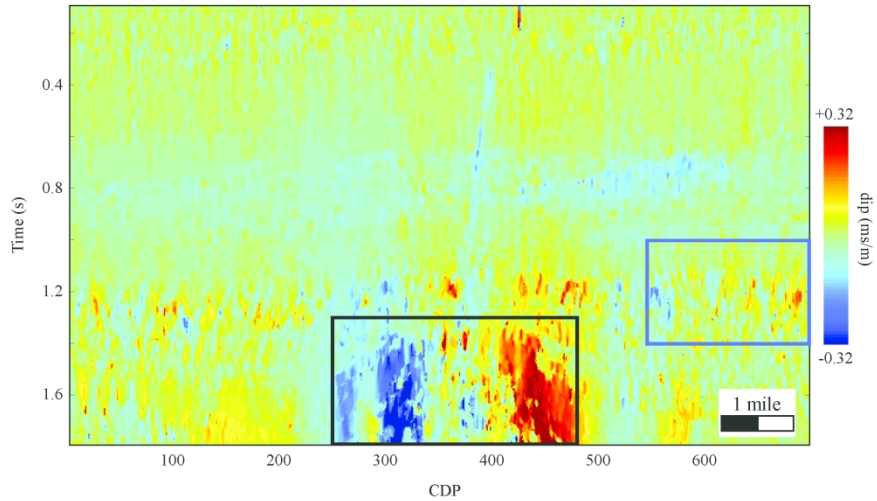
Figure 9a.

Figure 9a. Compare estimated crossline dip of different methods for the inline seismic section in Figure 8. Dip estimations based on (a) semblance scanning method, (b) GST analysis, and (c) our proposed method. Black and blue rectangles are two representative reflection features used to illustrate the superiority of our method.

254x190mm (300 x 300 DPI)
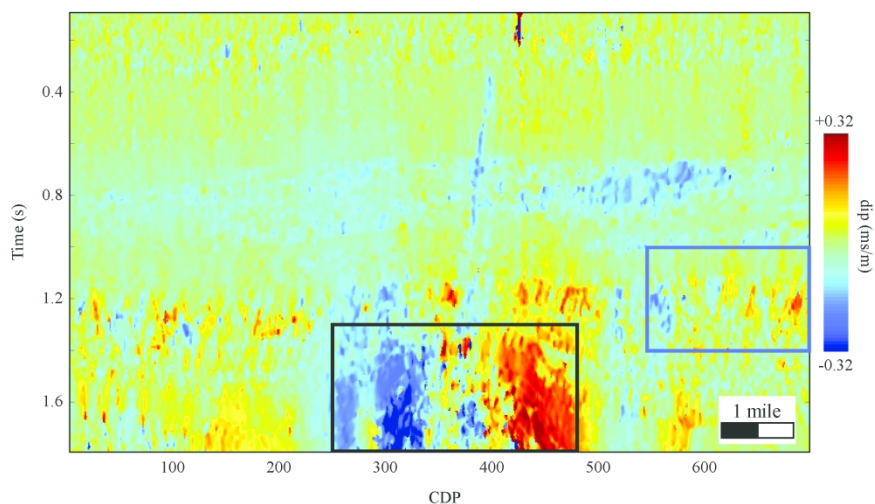
Figure 9b.

Figure 9b. Compare estimated crossline dip of different methods for the inline seismic section in Figure 8. Dip estimations based on (a) semblance scanning method, (b) GST analysis, and (c) our proposed method. Black and blue rectangles are two representative reflection features used to illustrate the superiority of our method.

254x190mm (300 x 300 DPI)
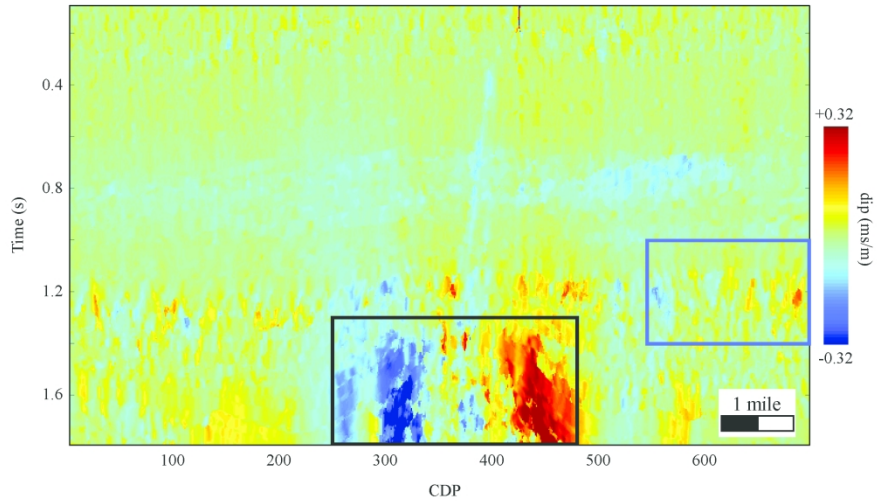
Figure 9c.

Figure 9c. Compare estimated crossline dip of different methods for the inline seismic section in Figure 8. Dip estimations based on (a) semblance scanning method, (b) GST analysis, and (c) our proposed method. Black and blue rectangles are two representative reflection features used to illustrate the superiority of our method.

254x190mm (300 x 300 DPI)
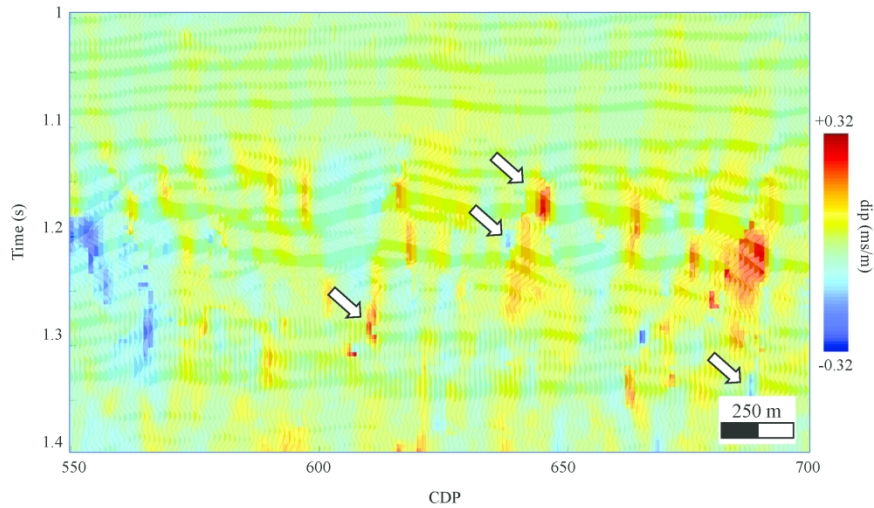
Figure 10a.

Figure 10a. The zoomed-in estimated dip in the blue rectangle in Figure 9 overlay on the zoomed-in seismic section in the blue box in Figure 8. Dip estimations based on (a) semblance scanning method, (b) GST analysis, and (c) our proposed method. White arrows in Figure 10a indicate estimated dip smears across discontinuous zones. Red arrow in Figure 10b indicates the inaccurate dip estimation. Red and white arrows in Figure 10c indicate our method accurately estimates the reflectors dip near discontinuous zones.

254x190mm (300 x 300 DPI)
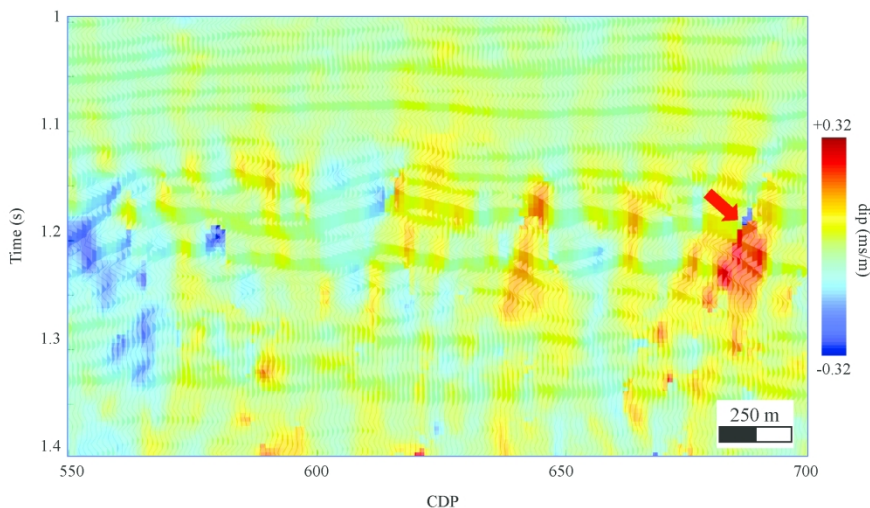
Figure 10b.

Figure 10b. The zoomed-in estimated dip in the blue rectangle in Figure 9 overlay on the zoomed-in seismic section in the blue box in Figure 8. Dip estimations based on (a) semblance scanning method, (b) GST analysis, and (c) our proposed method. White arrows in Figure 10a indicate estimated dip smears across discontinuous zones. Red arrow in Figure 10b indicates the inaccurate dip estimation. Red and white arrows in Figure 10c indicate our method accurately estimates the reflectors dip near discontinuous zones.

254x190mm (300 x 300 DPI)
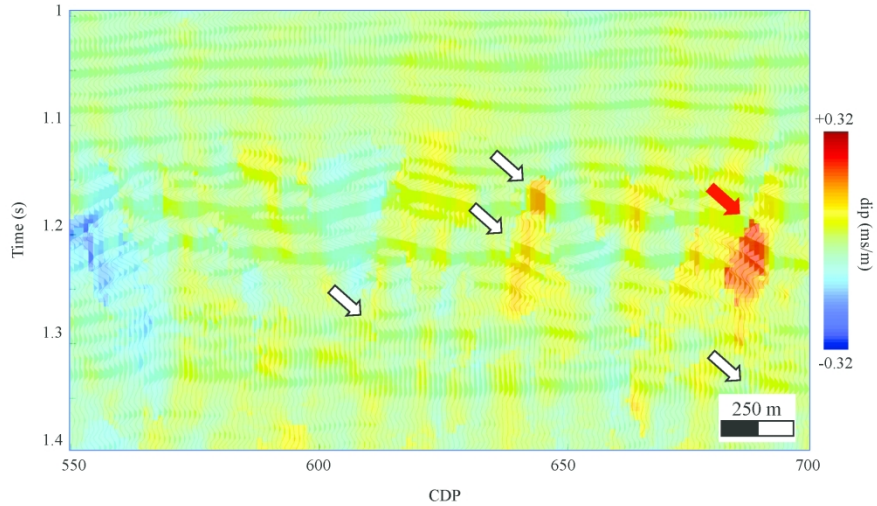
Figure 10c.

Figure 10c. The zoomed-in estimated dip in the blue rectangle in Figure 9 overlay on the zoomed-in seismic section in the blue box in Figure 8. Dip estimations based on (a) semblance scanning method, (b) GST analysis, and (c) our proposed method. White arrows in Figure 10a indicate estimated dip smears across discontinuous zones. Red arrow in Figure 10b indicates the inaccurate dip estimation. Red and white arrows in Figure 10c indicate our method accurately estimates the reflectors dip near discontinuous zones.

254x190mm (300 x 300 DPI)
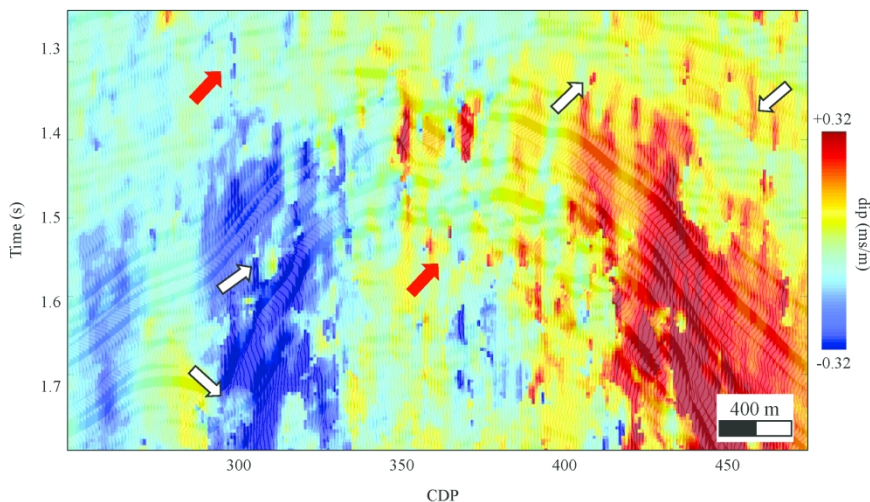
Figure 11a.

Figure 11a. The zoomed-in estimated dip in the black rectangle in Figure 9 overlay on the zoomed-in seismic section in the black box in Figure 8. Dip estimations based on (a) semblance scanning method, (b) GST analysis, and (c) our proposed method. White and red arrows in Figure 11a indicate inaccurate estimated dips and artifacts, respectively. Purple and white arrows in Figure 11b indicate seismic reflections should have the same color, and almost the same color, respectively. The arrows in Figure 11c indicate our method accurately estimates the reflectors dip.

254x190mm (300 x 300 DPI)
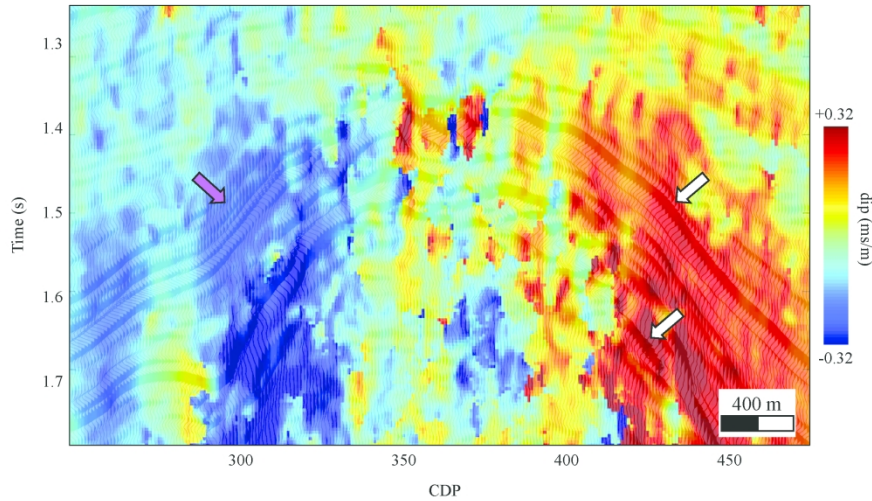
Figure 11b.

Figure 11b. The zoomed-in estimated dip in the black rectangle in Figure 9 overlay on the zoomed-in seismic section in the black box in Figure 8. Dip estimations based on (a) semblance scanning method, (b) GST analysis, and (c) our proposed method. White and red arrows in Figure 11a indicate inaccurate estimated dips and artifacts, respectively. Purple and white arrows in Figure 11b indicate seismic reflections should have the same color, and almost the same color, respectively. The arrows in Figure 11c indicate our method accurately estimates the reflectors dip.

254x190mm (300 x 300 DPI)
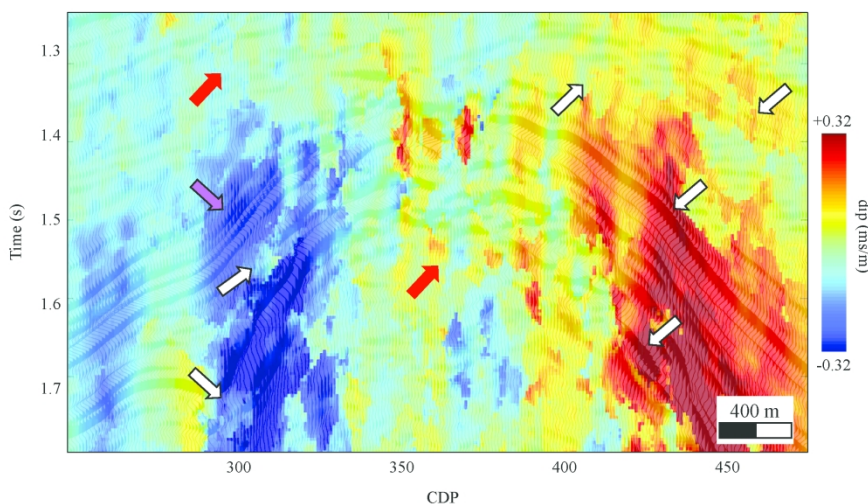
Figure 11c.

Figure 11c. The zoomed-in estimated dip in the black rectangle in Figure 9 overlay on the zoomed-in seismic section in the black box in Figure 8. Dip estimations based on (a) semblance scanning method, (b) GST analysis, and (c) our proposed method. White and red arrows in Figure 11a indicate inaccurate estimated dips and artifacts, respectively. Purple and white arrows in Figure 11b indicate seismic reflections should have the same color, and almost the same color, respectively. The arrows in Figure 11c indicate our method accurately estimates the reflectors dip.

254x190mm (300 x 300 DPI)
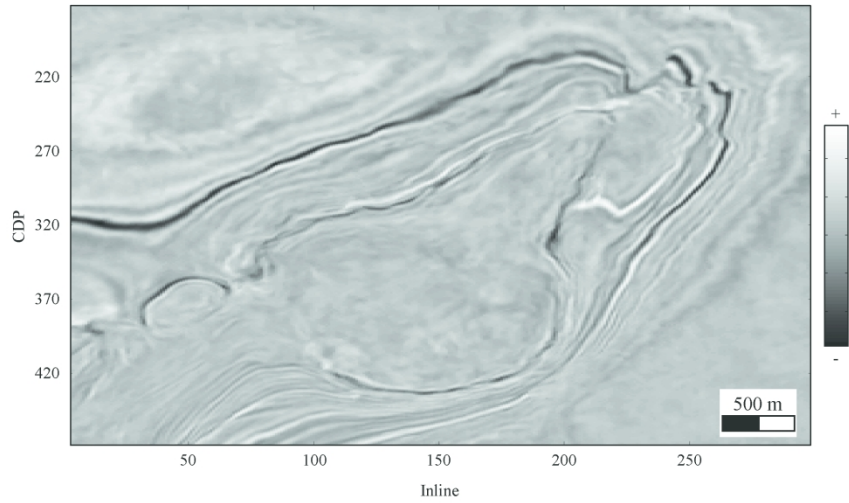
Figure 12.

Figure 12. The representative time slice seismic dataset at 1650ms.

254x190mm (300 x 300 DPI)
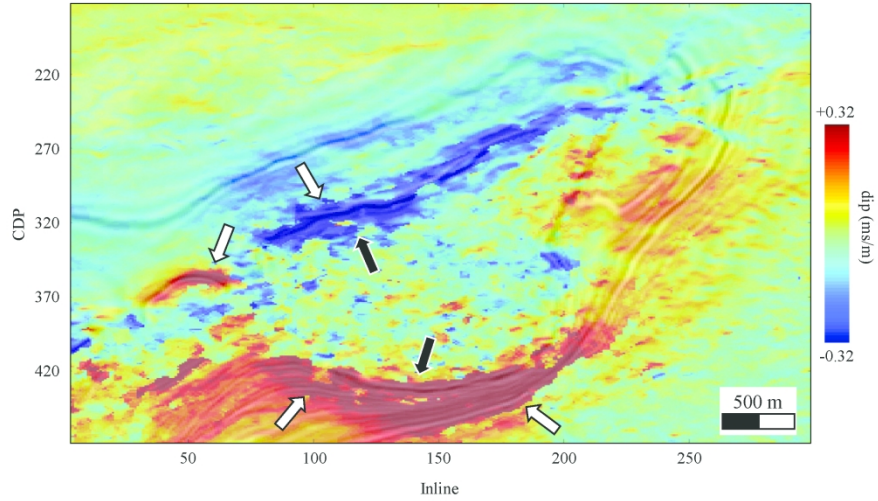
Figure 13a.

Figure 13a. Time slice at 1650ms from the crossline dip volume (equivalent to the time slice in Figure 12).
Dip estimations based on (a) semblance scanning method, (b) GST analysis, and (c) our proposed method.
White and black arrows indicate steep reflections, and locations with noise, respectively.

254x190mm (300 x 300 DPI)
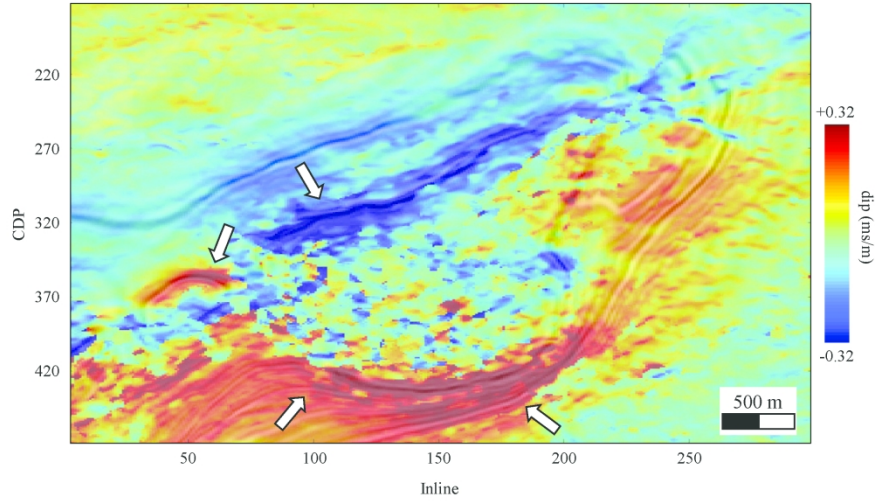
Figure 13b.

Figure 13b. Time slice at 1650ms from the crossline dip volume (equivalent to the time slice in Figure 12). Dip estimations based on (a) semblance scanning method, (b) GST analysis, and (c) our proposed method. White and black arrows indicate steep reflections, and locations with noise, respectively.

254x190mm (300 x 300 DPI)
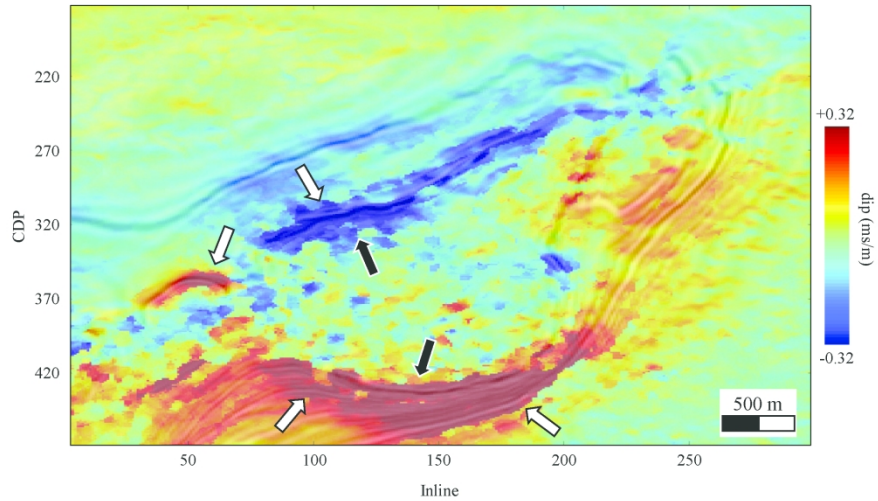
Figure 13c.

Figure 13c. Time slice at 1650ms from the crossline dip volume (equivalent to the time slice in Figure 12). Dip estimations based on (a) semblance scanning method, (b) GST analysis, and (c) our proposed method. White and black arrows indicate steep reflections, and locations with noise, respectively.

254x190mm (300 x 300 DPI)
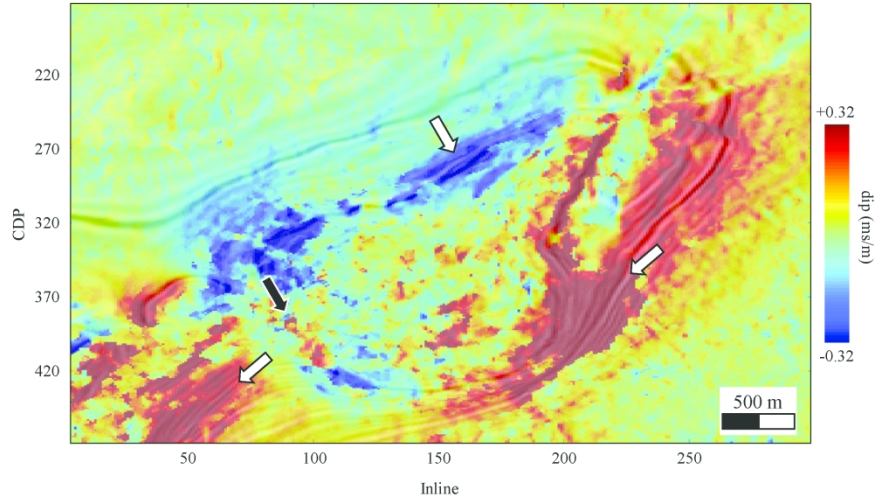
Figure 14a.

Figure 14a. Time slice at 1650ms from the inline dip volume (equivalent to the time slice in Figure 12). Dip estimations based on (a) semblance scanning method, (b) GST analysis, and (c) our proposed method. White and black arrows indicate steep reflections, and locations with noise, respectively.

254x190mm (300 x 300 DPI)
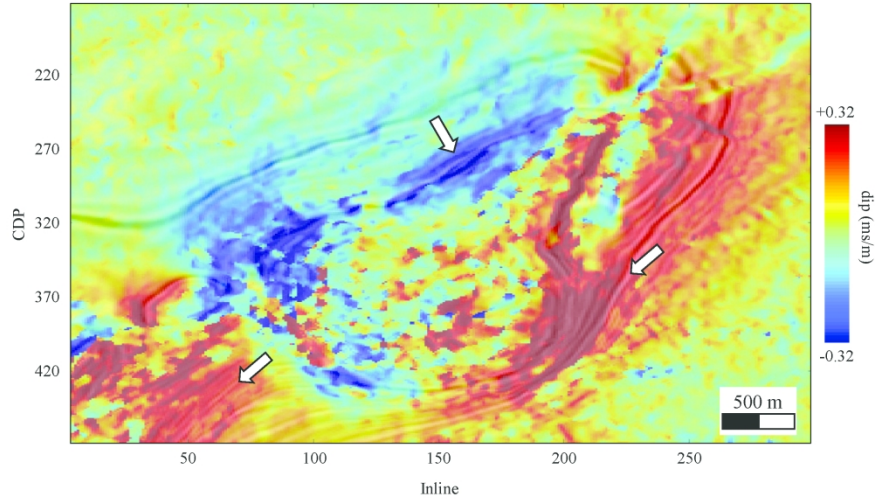
Figure 14b.

Figure 14b. Time slice at 1650ms from the inline dip volume (equivalent to the time slice in Figure 12). Dip estimations based on (a) semblance scanning method, (b) GST analysis, and (c) our proposed method. White and black arrows indicate steep reflections, and locations with noise, respectively.

254x190mm (300 x 300 DPI)
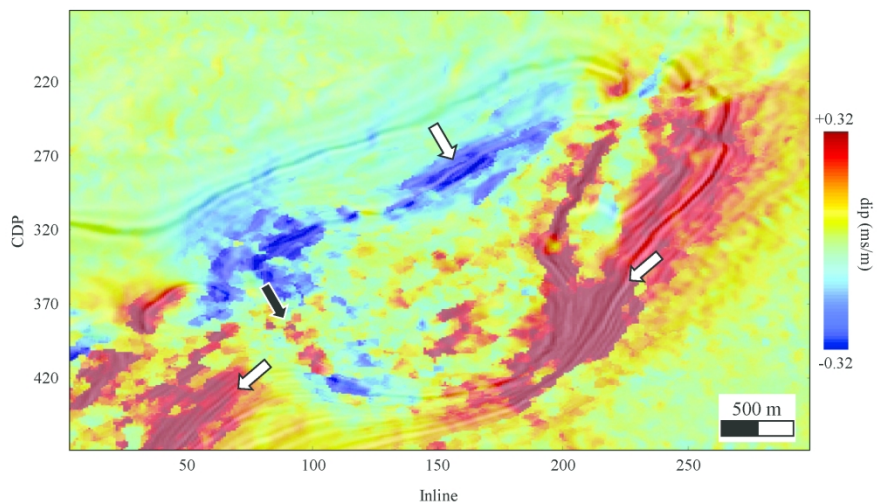
Figure 14c.

Figure 14c. Time slice at 1650ms from the inline dip volume (equivalent to the time slice in Figure 12). Dip estimations based on (a) semblance scanning method, (b) GST analysis, and (c) our proposed method. White and black arrows indicate steep reflections, and locations with noise, respectively.

254x190mm (300 x 300 DPI)
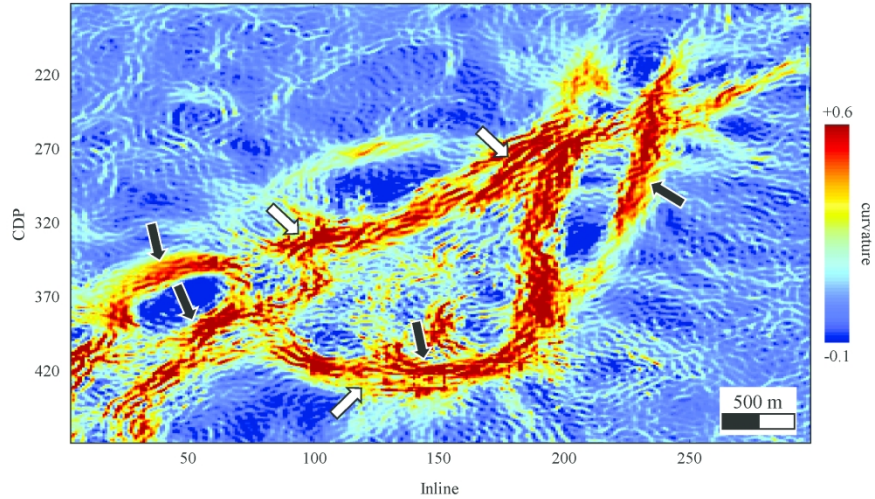
Figure 15a.

Figure 15a. Time slice at 1650ms from the most positive curvature volume (equivalent to the time slice in Figure 12). The most positive curvature based on the dip computed using (a) semblance scanning method, (b) GST analysis, and (c) our proposed method. White and black arrows indicate representative locations at the salt dome boundary.

254x190mm (300 x 300 DPI)
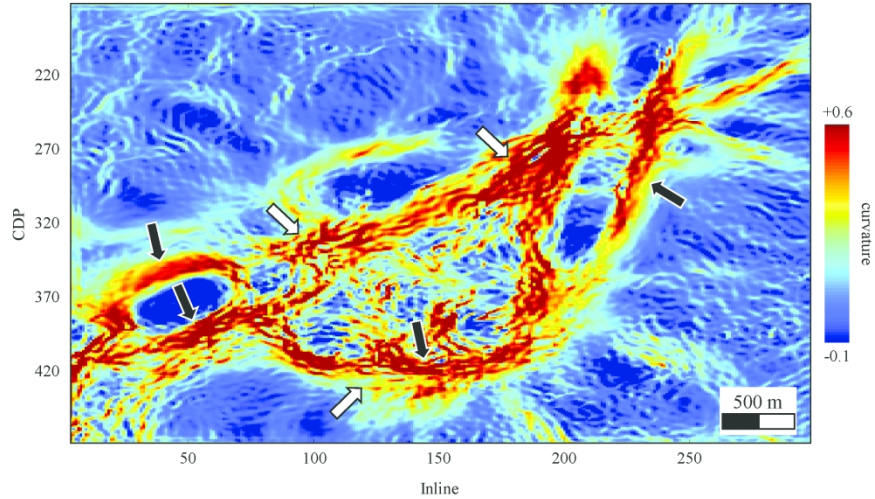
Figure 15b.

Figure 15b. Time slice at 1650ms from the most positive curvature volume (equivalent to the time slice in Figure 12). The most positive curvature based on the dip computed using (a) semblance scanning method, (b) GST analysis, and (c) our proposed method. White and black arrows indicate representative locations at the salt dome boundary.

254x190mm (300 x 300 DPI)
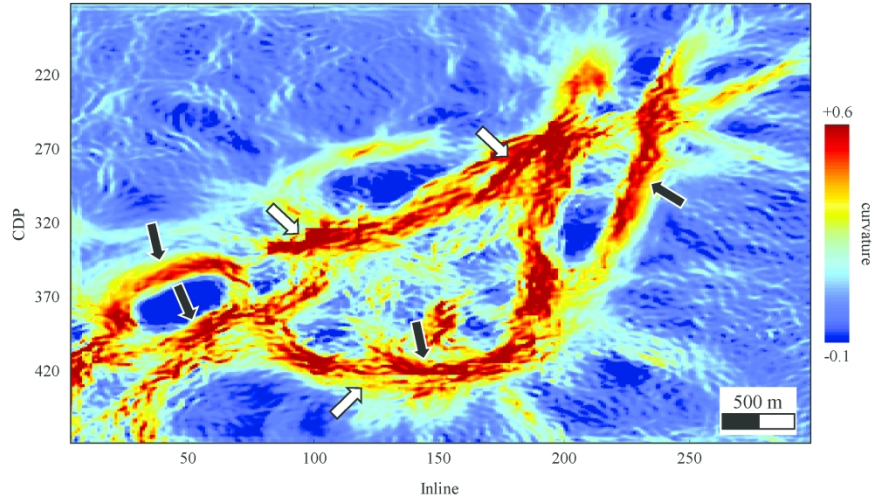
Figure 15c.

Figure 15c. Time slice at 1650ms from the most positive curvature volume (equivalent to the time slice in Figure 12). The most positive curvature based on the dip computed using (a) semblance scanning method, (b) GST analysis, and (c) our proposed method. White and black arrows indicate representative locations at the salt dome boundary.

254x190mm (300 x 300 DPI)

DATA AND MATERIALS AVAILABILITY

Data associated with this research are available and can be accessed via the following URL:lt;brgt; Note: A digital object identifier (DOI) linking to the data in a general or discipline-specific data repository is strongly preferred.